This is a repository copy of *Electronic Properties of {111} Twin Boundaries in a Mixed-Ion Lead Halide Perovskite Solar Absorber*.
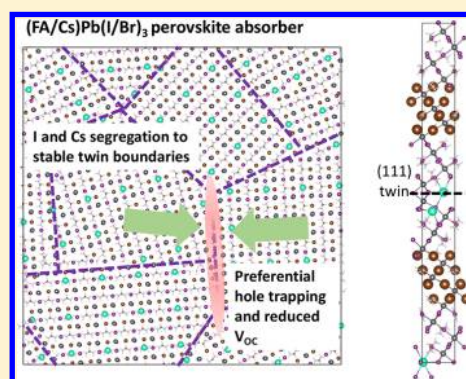
Article:

Electronic Properties of {111} Twin Boundaries in a Mixed-Ion Lead Halide Perovskite Solar Absorber

Keith P. McKenna*

Department of Physics, University of York, Heslington, York YO10 5DD, United Kingdom

S *Supporting Information*

ABSTRACT: We present first-principles theoretical predictions of the electronic properties of {111} twin boundaries in pure formamidinium lead iodide (FAPI) as well as a mixed-ion lead halide perovskite containing formamidinium, Cs, I, and Br. We find that the {111} twin boundary is extremely stable in pure FAPI but introduces no electron or hole trapping states and presents relatively small barriers (<100 meV) to transport of electrons and holes, suggesting that they are relatively benign for solar cell performance. However, in the mixed-ion perovskite, twin boundaries serve as a nucleation site for formation of an I- and Cs-rich secondary phase. The reduced band gap in this segregated phase leads to hole trapping and is likely to enhance electron–hole recombination and lead to reduced open-circuit voltage in solar cell devices. These results highlight the role of twin defects as nucleation sites for secondary phases, which can be extremely detrimental to solar cell performance.

Metal halide perovskites have been the focus of considerable research interest as high-mobility, defect-tolerant, and inexpensive thin-film solar absorber materials.[1] The metal halide perovskites have the general formula ABX$_3$, where the A site is a monovalent cation (typically methylammonium (MA), formamidinium (FA), or Cs), the B site is a divalent cation (typically Pb or Sn), and the X site is a halide anion (e.g., I, Br, or Cl). The ability to tune the band gap and other key properties of this class of materials by mixing ions on different sublattices has been demonstrated in a number of recent studies and opens up wide-ranging applications in optoelectronics (including solar cells and lasers).[2] In particular, absorbers with the composition FA$_{1-x}$Cs$_x$Pb(I$_{1-y}$Br$_y$)$_3$ have shown enhanced stability and efficiency for both tandem and single-junction solar cells.[2,3] On the other hand, there have been numerous recent reports suggesting that phase separation in multicomponent metal halide perovskites may be detrimental to performance.[4,5] To further complicate matters, although these materials are usually polycrystalline, the role of extended defects such as grain boundaries, twins, and stacking faults, remains poorly understood and a subject of much speculation.[6] Even for the much simpler pure MAPbI$_3$ phase, there are separate experimental studies suggesting that extended defects can both provide an efficient separation of electrons and holes as well as be responsible for increased nonradiative recombination.[7-10] There have been relatively few theoretical predictions of extended defect properties, and these have thus far mainly

focused on MAPbI$_3$ grain boundaries and associated intrinsic defects.[11,12] There are no theoretical studies of FA-based perovskites and the effect of cation and anion substitutions. This is particularly important in light of recent reports suggesting that grain boundaries may act as natural nucleation sites for secondary phase formation leading to increased electron–hole recombination.[5,13-16]

In this Letter, we present a theoretical investigation of the structural and electronic properties of twin defects in formamidinium-based lead halide perovskites. We employ density functional theory (DFT) methods similar to those previously applied to model extended defects in a range of other materials including CZTS, TiO$_2$, and Fe$_3$O$_4$.[17-19] We focus on the Σ3 (111) twin boundary (TB) defect, which we find has a very low formation energy in the cubic FAPI room-temperature phase.[20] As a consequence of their low energy, (111) TBs are predicted to be ubiquitous in pure FAPI. However, their electronic properties are benign for solar absorber applications, producing no new electronic states in the FAPbI$_3$ band gap and presenting very small barriers to intergrain electron and hole transport (<100 meV). We then consider the modification of FAPbI$_3$ upon introduction of Cs and Br on the A- and X-sites, respectively. Dilute Br and Cs show no strong tendency to segregate to the (111) TBs.

However, at compositions similar to those found to be beneficial for tandem cells (namely, $x = 0.125$ and $y = 0.333$), we find that there is strong cosegregation of I and Cs to the TB, leading to formation of an I-rich phase around the TB. The reduced band gap in this segregated phase leads to hole trapping states that are likely to enhance electron–hole recombination and also lead to reduced open-circuit voltage in devices. These results highlight the fact that TB defects in metal halide perovskites can be extremely stable and can serve as nucleation sites for secondary phase formation in mixed-ion perovskites that are extremely detrimental to material performance.

We model the FAPbI$_3$ $\Sigma3$ (111) TB using DFT as described in the Computational Methods section. The optimized structure of the supercell is shown in Figure 1a. The most
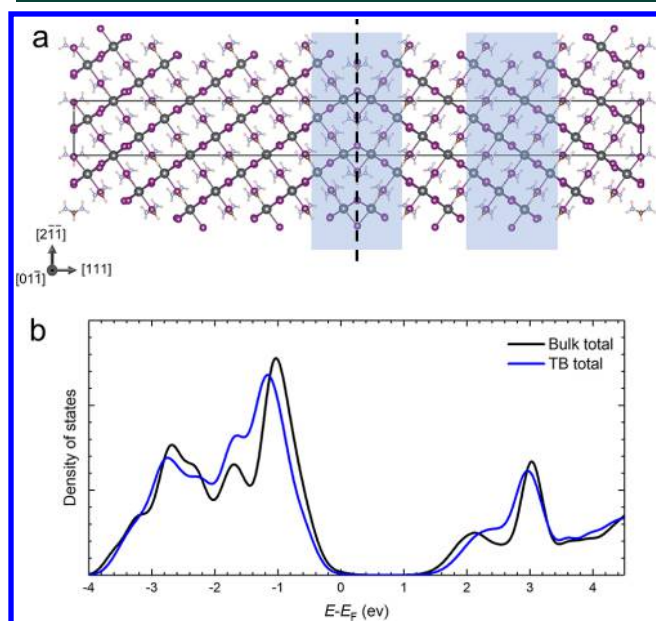

Figure 1. (a) Supercell used to model the atomic structure of the $\Sigma3$ (111) TB in FAPbI$_3$. One of the two symmetrically equivalent TB planes is highlighted with a dashed line. The following colors are used to represent the different species: C (brown), N (blue), H (pink), Pb (silver), and I (purple). (b) Density of states projected in the bulk-like and TB shaded regions shown in (a).

stable orientation of the FA ion at the TB is an average of the orientations of FA in the respective grains. We note that this highly ordered configuration is an idealized zero-temperature configuration as, due to the low barriers to FA reorientation, FA ions are expected to be dynamically disordered at room temperature.[20,21] The FA ion carries a small dipole, which means that there is a small electric field of opposing direction within each of the grains. As a result, there is a small (<0.1 V) difference in electrostatic potential between the two TB planes. However, this has little effect on the computed properties (discussed below).

The TB formation energy is normally defined as

$$E_f = \frac{E_{TB} - NE_c}{2A}$$

where E_{TB} is the total energy of the fully optimized TB supercell, N is the number of formula units of FAPbI$_3$ in the TB supercell, E_c is the total energy of bulk cubic FAPbI$_3$ per formula unit, and A is the cross-sectional area of the TB

supercell. Using this formula, the calculated formation energy for the $\Sigma3$ (111) TB is $E_f = -0.12$ J m^{-2} (i.e., small and negative). With dispersion corrections included at the DFT-D3 level, the formation energy is similar at $E_f = -0.11$ J m^{-2}. We have checked carefully that this result is genuine and not an error due to poorly converged energies. While negative stacking fault energies and twin energies are rare, they have been observed previously in high-entropy alloys such as CrNiCo and FeCrNiCo.[22] It is important to remember that these are zero-temperature formation energies, and at finite temperature, the formation free energy (including vibrational and rotational contributions) may not be negative. Nevertheless, it suggests that such twins are highly stable in FAPbI$_3$ and, barring kinetic obstacles to their formation, should be prevalent in real materials. Indeed, this result is consistent with previous suggestions that FAPI may contain a large number of twins and stacking faults that can lead to incorrect assignment of crystal structure.[20,23]

To characterize the electronic structure of the TB, we calculate the density of states projected onto atoms in the vicinity of the TB and in the bulk (Figure 1b). As mentioned above, there is a small difference in the electrostatic potential between the two TBs in the supercell. However, there are no significant differences in the projected density of states (PDOS) for the two TBs near the valence and conduction bands. The PDOS for the bulk region is in good agreement with the calculated density of states for the bulk unit cell and exhibits a band gap of around 1.3 eV. The PDOS in the TB region has a slightly larger band gap. The valence band maximum (VBM) and conduction band minimum (CBM) lie slightly below and above those of the bulk PDOS. This suggests that there are no interface states that could present electron or hole traps.

The small difference (of the order 0.1 eV) between the band edges in the TB and bulk regions suggests that there is a relatively small barrier to electron and hole transport across the TB. To characterize this more precisely, we calculate the two-dimensional band structure (corresponding to different in-plane crystal momenta $k_∥$) for the TB supercell and for a corresponding bulk supercell of the same dimensions. The eigenvalues obtained in the two calculations are aligned to a common energy scale using bulk core levels as a reference (requiring a relative shift of 0.04 eV). Figure 2 shows the calculated band structures and corresponding minimum barriers for both electrons and holes (estimated as the energy difference between the respective VBMs and CBMs). At the Γ point (corresponding to electrons propagating normal to the TB), the barrier for electrons is around 80 meV, and for holes, it is around 30 meV. However, there is significant variation of the barrier depending on $k_∥$. For holes, the barrier reduces to zero for many values of $k_∥$, whereas for electrons, it is always finite and can reach over 100 meV near the X-point.

To assess the tendency of Br$_I$ and Cs$_{FA}$ substitutional defects in FAPbI$_3$ to segregate to the TB, we calculated the total energy of isolated defects at different sites within the TB supercell. We then calculated the segregation energy (E_{seg}), defined as the total energy difference with respect to a bulk-like site in the center of the grain (15 Å away from TB). Figure 3 shows the calculated segregation energy for both Br$_I$ and Cs$_{FA}$. For Br, away from the TB plane, there is a repeating pattern of three inequivalent I sites with a site-to-site variation in stability of the order 0.1 eV. Within 5 Å of the TB plane, there is a noticeable modification of this pattern; however, there are no
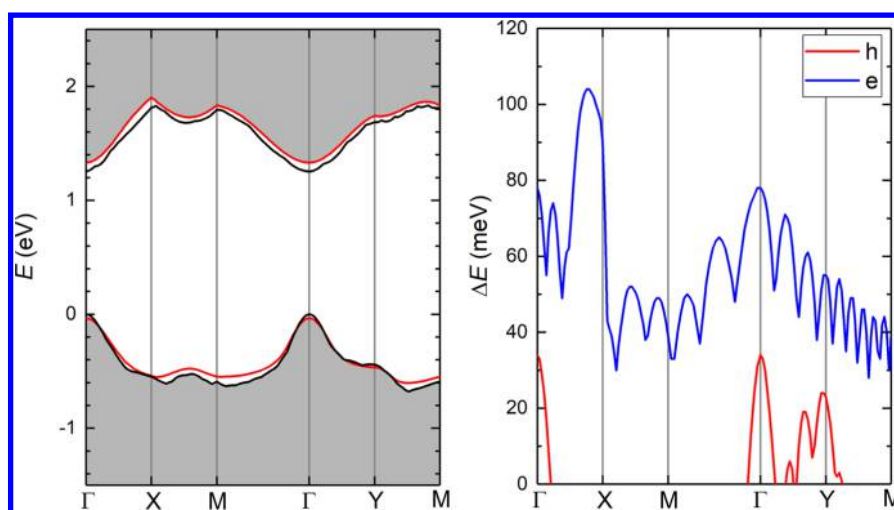
Figure 2. (left) Interfacial band structure for the $\Sigma 3$ (111) TB in FAPbI$_3$. The black and red lines represent the bulk and TB VBM and CBM, respectively. The k-points are defined as Γ (0,0,0), X ($\frac{\pi}{a}$, 0, 0), M ($\frac{\pi}{a}$, $\frac{\pi}{a}$, 0) and Y (0,0, $\frac{\pi}{a}$, 0). (right) Minimum barrier (ΔE) for electrons (blue) and holes (red) to pass through the TB.
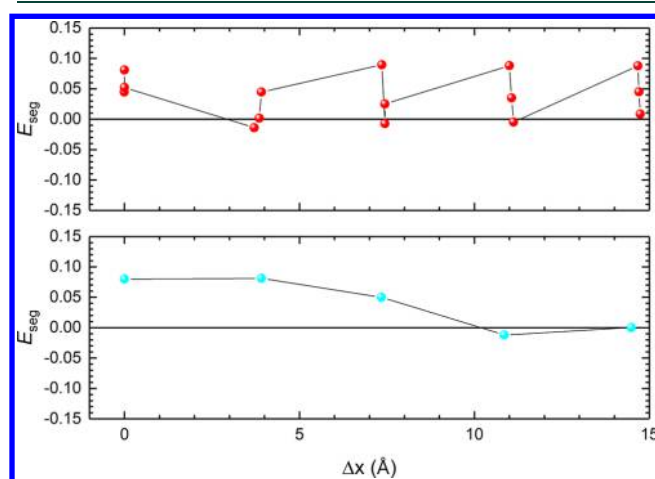

Figure 3. Calculated segregation energy (E_{seg}) for (top) a single Br ion substituting for I [Br$_I$] and (bottom) a single Cs ion substituting for FA [Cs$_{FA}$] as a function of distance from the TB (Δx).

sites near the TB that are significantly more stable than those in the bulk. Therefore, we predict no strong segregation of dilute Br$_I$ defects to the TB. For Cs, sites near the TB are nearly 0.1 eV less stable than those in the bulk. Again, this suggests that there is no strong segregation of dilute Cs$_{FA}$ defects to the TB either. We also computed the density of states for the defect supercells and found that these substitutional defects do not introduce any states inside of the fundamental band gap for low concentrations (see the PDOS plots in the Figures S1 and S2).

We now turn to address the effect of increased loading of Cs and Br. In particular, we consider the composition FA$_{0.875}$Cs$_{0.125}$Pb(I$_{0.666}$Br$_{0.333}$)$_3$, which is close to that identified as particularly promising in experimental studies and convenient for theoretical calculations. As described in the Computational Methods section, we construct a $2 \times 2 \times 2$ cubic supercell (with composition FA$_7$Cs$_1$Pb$_8$I$_{16}$Br$_8$) to model the bulk phase obtaining a lattice constant of 6.33 Å and a band gap of 1.6 eV. On the basis of only total energies (rather than free energies), we predict that this composition is

metastable, with phase separation into CsPbBr$_3$ (12.5%), FAPbI$_3$ (66.7%), and FAPbBr$_3$ (20.8%) favorable by 0.09 eV per formula unit. A full assessment of stability would require statistical treatment, such as that recently carried out for Cs-based metal halide perovskites, but is beyond the scope of this work, which is focused on the properties of TB defects.[16]

To model the properties of the TB in the mixed-ion perovskite, we constructed a TB supercell similar to that shown in Figure 1 with the composition FA$_{19}$Cs$_3$Pb$_{22}$I$_{44}$Br$_{22}$ (corresponding to x = 0.158 and y = 0.666). The supercell dimensions are scaled according to the optimized bulk lattice constant obtained above. We then considered various distributions of the Cs and Br ions within the supercell, as shown in Figure 4: (a) homogeneous distribution of Br and Cs, (b) homogeneous Cs/Br segregated to TB, (c) Br and Cs segregated to TB, (d) homogeneous Cs/I segregated to TB, and (e) I and Cs segregated to TB. The optimized structures for these different atomic configurations were then obtained. We found that the structure with I and Cs cosegregated to the TB was nearly 2 eV more stable than the homogeneous arrangement. Effectively, this corresponds to phase separation into FAPbBr$_3$ in the center of the grains, CsPbI$_3$ at the TB plane, and FAPbI$_3$ in the regions adjacent to the TB. For comparison a similar phase separation in the bulk reduces the total energy less than 0.7 eV, highlighting the role of the TB as a nucleation site for phase separation. The calculated relative energies of these different configurations are only slightly modified upon inclusion of dispersion corrections at the DFT-D3 level (see Figure 4). The formation energies of supercells considered in this work are also given with respect to the energy of the pure perovskite compositions CsPbBr$_3$, FAPbI$_3$, and FAPbBr$_3$ in Table S1.

Finally, we address the electronic properties of the most stable TB supercell by computing the PDOS in the bulk and TB regions. As shown in Figure 5a, the local band gap at the TB is significantly smaller than that in the bulk. This can be understood because the bulk region is primarily FAPbBr$_3$ while the TB region is primarily FAPbI$_3$. The VBM at the TB is around 0.2 eV higher than that in the bulk, while the CBM for the bulk and TB are similar. This suggests that photoexcited holes will preferentially localize near the TB, while electrons
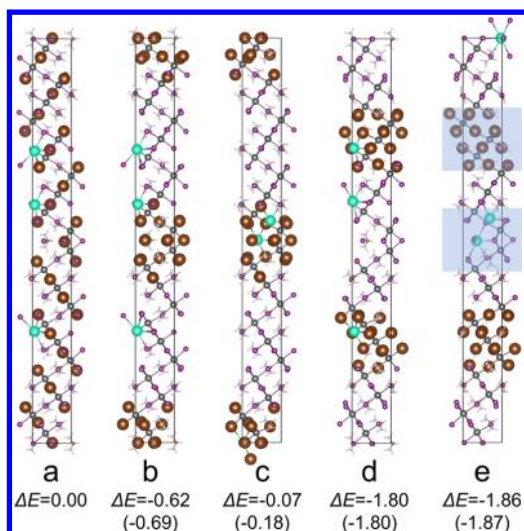
Figure 4. Optimized structure of the TB for different arrangements of Cs and FA on the cation sublattice and I and Br on the halide ion sublattice along with their relative energies in eV (relative energies including dispersion corrections at the DFT-D3 level are included in brackets). (a) Homogeneous distribution of Br and Cs, (b) homogeneous Cs/Br segregated to TB, (c) Br and Cs segregated to TB, (d) homogeneous Cs/I segregated to TB, and (e) I and Cs segregated to TB. The following colors are used to represent the different species: C (brown), N (blue), H (pink), Cs (turquoise), Pb (silver), I (purple), and Br (brown). The Br and Cs ions are represented with larger spheres in these figures to aid visualization of their spatial distribution. Shaded areas represent regions used for the PDOS calculation in Figure 5a.
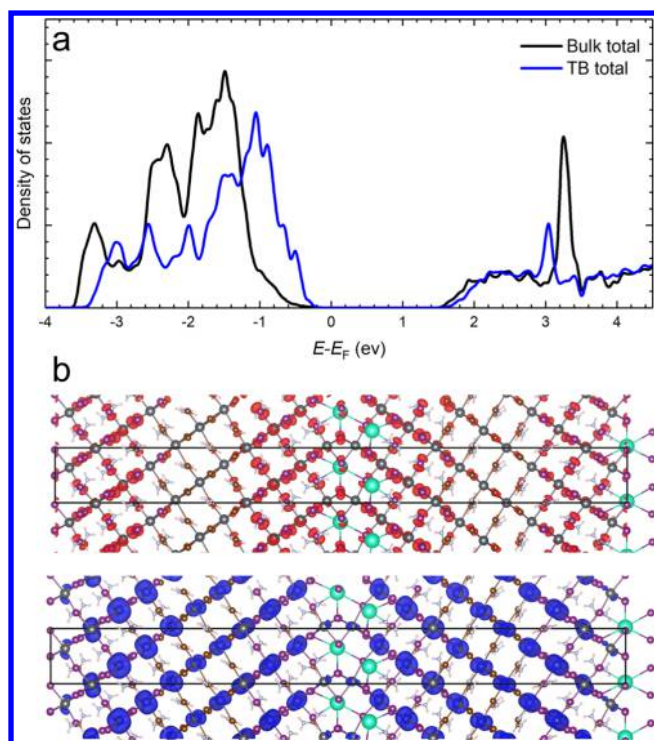

Figure 5. (a) Density of states projected in the bulk-like and TB shaded regions shown in Figure 4e. (b) Electron (top) and hole (bottom) spin density isosurfaces for vertically photoexcited charge carriers in the phase-separated mixed-ion perovskite.

will be less affected by variations in composition near to the TBs. This is likely to lead to a significant reduction in the open-circuit voltage and also lead to increased electron–hole recombination.

To provide further insight into the localization of photo-excited electrons and holes in TB, we show spin density isosurfaces for vertically added electron and holes (Figure 5b). The hole density is clearly localized in the FAPbI$_3$ region adjacent to the TB as well as the TB plane itself. The electron density is delocalized across both the bulk FAPbBr$_3$ and TB FAPbI$_3$ regions with much less contribution on the TB plane (which is both Cs- and I-rich).

The results presented above have been obtained using DFT and the PBESol approximation to exchange and correlation. Scalar relativistic effects are included, but the spin–orbit (SO) interaction that is important for the heavy Pb atom is omitted. Previous studies have shown that to obtain an accurate band structure one requires SO in conjunction with either GW or a nonlocal functional.[24] Such approaches would be too expensive computationally for the size of supercells used here. However, due to a cancellation of errors, one can get a reasonable semiquantitative description of the band structure using only the PBESol functional.[25] We performed calculations of the density of states including SO coupling for both the pristine FAPbI$_3$ TB and the most stable mixed-ion TB to test this. As shown in Figures S3 and S4, while the band gap is reduced, the key features of the electronic structure are unchanged. Importantly, for the present results, it is the relative difference in band gaps and stability that are most important. Therefore, we believe that our main results and conclusions should be robust.

In modeling the TB in the mixed-ion lead halide perovskite, it is not computationally feasible to consider all possible atomic configurations, but we have considered a large number of possible atomic arrangements representative of different types of behavior. We have restricted attention to configurations that retain the underlying perovskite structure. However, it is, in principle, possible for secondary phases to adopt different structures (such as PdI$_2$). In this respect, our models are most appropriate to relatively low temperature processing where ion migration is facilitated by vacancies on the A- and X-sublattices.[26] In such a situation, one can expect the homogeneously mixed phase to be metastable but over time (or with increased temperature) may phase-separate, leading to growth of FAPbI$_3$-rich regions adjacent to TBs. We predict that such a scenario would lead to progressive deterioration of device efficiency through reduction of open-circuit voltage and increased recombination.

There is a great deal of experimental evidence for the formation of I-rich phases in mixed-halide perovskites.[5,13–15] For example, irradiation of mixed Br and I perovskite phases leads to red-shifted photoluminescence spectra attributed to luminescence from I-rich domains.[27–30] While extended defects are often suggested to be important, their precise role has proved difficult to pinpoint. Our theoretical models provide insight into these issues and suggest that highly stable TB defects may provide a natural nucleation site for I-rich secondary phases with reduced band gap.

In summary, we have investigated the structure, stability, and electronic properties of the $\Sigma 3$ (111) TB in pure FAPI as well a mixed phase involving addition of Cs and Br. We predict that the TB is extremely stable and so should be prevalent in real materials but is relatively benign in pure FAPbI$_3$ (presenting

relatively small barriers to intergrain electron and hole transport (less than 0.1 eV) and no deep trap states). However, in the mixed-ion perovskite—specifically $FA_{0.875}Cs_{0.125}Pb (I_{0.666}Br_{0.333})_3$—we find that the TB serves as a natural necleation site for segregation of an I- and Cs-rich phase. The I-rich phase has a reduced band gap compared to the bulk and serves as a preferential trap for photoexcited holes. The formation of the I-rich phase at the TB, which may be faciliated by mobile halide ion vacancies even at relatively low temperature,[26] is expected to enhance electron–hole recombinaton and also lead to reduced open-circuit voltage in devices.

The (111) TB is an important defect due to its very high stability; however, more generally, perovskite absorbers are usually polycrystalline and contain a wider range of extended defects (including grain boundaries with higher formation energies and much lower symmetry). Such defects may present even stronger tendencies to nucleate secondary phases and modify electronic properties. While mixed-ion perovskites offer tremendous opportunities for tuning properties, they also present a considerable challenge in ensuring they remain stable and retain their desirable electronic proterties in the presence of extended defects. The present work provides atomistic insight into some of these effects, but much more remains to be done, requiring advances in theoretical modeling and experimental characterization, to both understand and learn how to control extended defects to optimize materials performance for solar cell applications.

■ COMPUTATIONAL METHODS

Spin-polarized DFT calculations were carried out using the Vienna ab initio simulation package (VASP).[31,32] We employed the projector augmented wave method, and the following electrons were treated as valence: C (2s and 2p), N (2s and 2p), H (1s), Cs (5s, 5p, and 6s), Pb (5d, 6s, and 6p), I (5s and 5p), and Br(4s and 4p) and expanded in a plane wave basis set (500 eV cutoff). The PBESol functional[33] was used to approximate exchange and correlation, which has been demonstrated previously to yield lattice constants and band gaps in close agreement with experiment.[25] Bulk $FAPbI_3$ was modeled using a cubic unit cell and a $10 \times 10 \times 10$ Monkhorst−Pack k-point sampling scheme (ensuring that the R-point is included).[20,21,25] Structures were optimized to a force tolerance of 10 meV/Å, yielding a predicted lattice constant of $a = 6.35$ Å for bulk $FAPbI_3$ and a band gap of 1.3 eV (in close agreement with the experimentally determined lattice constant of 6.36 Å[20] and band gap of 1.5 eV[34]). We also calculated total energies with dispresion corrections (at the DFT-D3 level) using the PBE optimized geometries.[35] As discussed in previous studies, the use of semilocal exchange and the omission of SO coupling leads to a cancellation of errors, resulting in a reasonable prediction of band gap for lead halide perovskites.[25]

To model the mixed perovskite phase with composition $FA_{0.872}Cs_{0.125}Pb (I_{0.666}Br_{0.333})_3$, we constructed a $2 \times 2 \times 2$ supercell expansion of the conventional cubic FAPI unit cell. The Monkhorst−Pack k-point sampling was reduced to $3 \times 3 \times 3$, and the structure was optimized with respect to the coordinates of all atoms and the cell volume. The resulting lattice constant and band gap were 6.33 Å and 1.6 eV (compared to around 6.25 Å and 1.7 eV experimentally).

To model the $\Sigma 3$ (111) TB, we employed methods similar to those previously described in applications to a range of materials including silicon, MgO, HfO_2, and TiO_2.[18,36−38] In particular, we constructed supercells that contained two mirror-symmetric grains separated by at least 40 Å to minimize interactions between the periodically repeated TBs. We based the initial structure of the $\Sigma 3$ (111) TB on the structurally similar perovskite $SrTiO_3$.[39,40] The k-point sampling was reduced to $3 \times 3 \times 1$ for all of the TB supercell calculations, and the structure was optimized with respect to the coordinates of all atoms. A number of different options for the orientation of the FA ion on the TB plane were considered in order to identify the most stable.

■ ASSOCIATED CONTENT

⑤ Supporting Information

The Supporting Information is available free of charge on the ACS Publications website at DOI: 10.1021/acsenergy-lett.8b01700.

> Density of states for the $FAPbI_3$ TB with single substitutional Br and CS ions, density of states for the pristine $FAPbI_3$ TB and heavily Cs- and Br-doped $FAPbI_3$ TB at the PBE-SOC level of theory, and formation energies for various supercells considered in this work with respect to the pure perovskite compositions $CsPbBr_3$, $FAPbI_3$ and $FAPbBr_3$ (PDF)

■ AUTHOR INFORMATION

Corresponding Author
*E-mail: keith.mckenna@york.ac.uk.

ORCID
Keith P. McKenna: 0000-0003-0975-3626

Notes
The author declares no competing financial interest.
All data created during this research are available by request from the University of York Research database at https://doi.org/10.15124/774b3572-7f18-48e2-ac90-6b95a261d016.

■ REFERENCES

(1) Egger, D. A.; Edri, E.; Cahen, D.; Hodes, G. Perovskite Solar Cells: Do We Know What We Do Not Know? *J. Phys. Chem. Lett.* **2015**, 6, 279−282.

(2) Bush, K. A.; Frohna, K.; Prasanna, R.; Beal, R. E.; Leijtens, T.; Swifter, S. A.; McGehee, M. D. Compositional Engineering for Efficient Wide Band Gap Perovskites with Improved Stability to Photoinduced Phase Seragration. *ACS Energy Lett.* **2018**, 3, 428−435.

(3) McMeekin, D. P.; Sadoughi, G.; Rehman, W.; Eperon, G. E.; Saliba, M.; Horantner, M. T.; Haghighirad, A.; Sakai, N.; Korte, L.; Rech, B.; et al. A Mixed-Cation Lead Halide Perovskite Absorber for Tandem Solar Cells. *Science* **2016**, 351, 151−155.

(4) Brennan, M. C.; Draguta, S.; Kamat, P. V.; Kuno, M. Light-Induced Anion Phase Segregation in Mixed Halide Perovskites. *ACS Energy Lett.* **2018**, 3, 204−213.

(5) Tang, X.; Van Den Berg, M.; Gu, E.; Horneber, A.; Matt, G. J.; Osvet, A.; Meixner, A. J.; Zhang, D.; Brabec, C. J. Local Observation of Phase Segregation in Mixed-Halide Perovskite. *Nano Lett.* **2018**, 18, 2172−2178.

(6) Ono, L. K.; Qi, Y. Surface and Interface Aspects of Organometal Halide Perovskite Materials and Solar Cells. *J. Phys. Chem. Lett.* **2016**, *7*, 4764−4794.

(7) Edri, E.; Kirmayer, S.; Henning, A.; Mukhopadhyay, S.; Gartsman, K.; Rosenwaks, Y.; Hodes, G.; Cahen, D. Why Lead Methylammonium Tri-Iodide Perovskite-Based Solar Cells Require a Mesoporous Electron Transporting Scaffold (but Not Necessarily a Hole Conductor). *Nano Lett.* **2014**, *14*, 1000−1004.

(8) Yun, J. S.; Ho-Baillie, A.; Huang, S.; Woo, S. H.; Heo, Y.; Seidel, J.; Huang, F.; Cheng, Y. B.; Green, M. A. Benefit of Grain Boundaries in Organic-Inorganic Halide Planar Perovskite Solar Cells. *J. Phys. Chem. Lett.* **2015**, *6*, 875−880.

(9) de Quilettes, D. W.; Vorpahl, S. M.; Stranks, S. D.; Nagaoka, H.; Eperon, G. E.; Ziffer, M. E.; Snaith, H. J.; Ginger, D. S. Impact of Microstructure on Local Carrier Lifetime in Perovskite Solar Cells. *Science* **2015**, *348*, 683−686.

(10) Yang, B.; Dyck, O.; Poplawsky, J.; Keum, J.; Puretzky, A.; Das, S.; Ivanov, I.; Rouleau, C.; Duscher, G.; Geohegan, D.; et al. Perovskite Solar Cells with Near 100% Internal Quantum Efficiency Based on Large Single Crystalline Grains and Vertical Bulk Heterojunctions. *J. Am. Chem. Soc.* **2015**, *137*, 9210−9213.

(11) Yin, W. J.; Shi, T.; Yan, Y. Unique Properties of Halide Perovskites as Possible Origins of the Superior Solar Cell Performance. *Adv. Mater.* **2014**, *26*, 4653−4658.

(12) Shan, W.; Saidi, W. A. Segregation of Native Defects to the Grain Boundaries in Methylammonium Lead Iodide Perovskite. *J. Phys. Chem. Lett.* **2017**, *8*, 5935−5942.

(13) Wang, L.; McCleese, C.; Kovalsky, A.; Zhao, Y.; Burda, C. Femtosecond Time-Resolved Transient Absorption Spectroscopy of $CH_3NH_3PbI_3$ Perovskite Films: Evidence for Passivation Effect of PbI_2. *J. Am. Chem. Soc.* **2014**, *136*, 12205−12208.

(14) Chen, Q.; Zhou, H.; Song, T.-b.; Luo, S.; Hong, Z.; et al. Controllable Self-Induced Passivation of Hybrid Lead Iodide Perovskites Toward High Performance Solar Cells. *Nano Lett.* **2014**, *14*, 4158−4163.

(15) Gomez, A.; Sanchez, S.; Campoy-Quiles, M.; Abate, A. Topological Distribution of Reversible and Non-Reversible Degradation in Perovskite Solar Cells. *Nano Energy* **2018**, *45*, 94−100.

(16) Bechtel, J. S.; Van der Ven, A. First-Principles Thermodynamics Study of Phase Stability in Inorganic Halide Perovskite Solid Solutions. *Phys. Rev. Mater.* **2018**, *2*, 045401.

(17) Mendis, B. G.; McKenna, K. P.; Gurieva, G.; Rumsey, M. S.; Schorr, S. Crystal Structure and Anti-Site Boundary Defect Characterisation of $Cu_2ZnSnSe_4$. *J. Mater. Chem. A* **2018**, *6*, 189−197.

(18) Wallace, S. K.; McKenna, K. P. Grain Boundary Controlled Electron Mobility in Polycrystalline Titanium Dioxide. *Adv. Mater. Interfaces* **2014**, *1*, 1400078.

(19) McKenna, K. P. Effect of Polaronic Charge Transfer on Band Alignment at the Cu/TiO_2 Interface. *Phys. Rev. B: Condens. Matter Mater. Phys.* **2016**, *94*, 155147.

(20) Weller, M. T.; Weber, O. J.; Frost, J. M.; Walsh, A. Cubic Perovskite Structure of Black Formamidinium Lead Iodide, α-$[HC(NH_2)_2]PbI_3$ at 298 K. *J. Phys. Chem. Lett.* **2015**, *6*, 3209−3212.

(21) Frost, J. M.; Walsh, A. What Is Moving in Hybrid Halide Perovskite Solar Cells? *Acc. Chem. Res.* **2016**, *49*, 528−535.

(22) Zhang, Y.; Zhuang, Y.; Hu, A.; Kai, J.; Liu, C. The Origin of Negative Stacking Fault Energies and Nano-Twin Formation in Face-Centered Cubic High Entropy Alloys. *Scr. Mater.* **2017**, *130*, 96−99.

(23) Németh, P.; Garvie, L. A. J.; Aoki, T.; Dubrovinskaia, N.; Dubrovinsky, L.; Buseck, P. R. Lonsdaleite is Faulted and Twinned Cubic Diamond and Does Not Exist as a Discrete Material. *Nat. Commun.* **2014**, *5*, 5447.

(24) Brivio, F.; Butler, K. T.; Walsh, A.; Van Schilfgaarde, M. Relativistic Quasiparticle Self-Consistent Electronic Structure of Hybrid Halide Perovskite Photovoltaic Absorbers. *Phys. Rev. B: Condens. Matter Mater. Phys.* **2014**, *89*, 1−6.

(25) Brivio, F.; Walker, A. B.; Walsh, A. Structural and Electronic Properties of Hybrid Perovskites for High-Efficiency Thin-Film Photovoltaics From First-Principles. *APL Mater.* **2013**, *1*, 042111.

(26) Azpiroz, J. M.; Mosconi, E.; Bisquert, J.; De Angelis, F. Defect Migration in Methylammonium Lead Iodide and its Role in Perovskite Solar Cell Operation. *Energy Environ. Sci.* **2015**, *8*, 2118−2127.

(27) Hoke, E. T.; Slotcavage, D. J.; Dohner, E. R.; Bowring, A. R.; Karunadasa, H. I.; McGehee, M. D. Reversible Photo-Induced Trap Formation in Mixed-Halide Hybrid Perovskites for Photovoltaics. *Chem. Sci.* **2015**, *6*, 613−617.

(28) Slotcavage, D. J.; Karunadasa, H. I.; McGehee, M. D. Light-Induced Phase Segregation in Halide-Perovskite Absorbers. *ACS Energy Lett.* **2016**, *1*, 1199−1205.

(29) Beal, R. E.; Slotcavage, D. J.; Leijtens, T.; Bowring, A. R.; Belisle, R. A.; Nguyen, W. H.; Burkhard, G. F.; Hoke, E. T.; McGehee, M. D. Cesium Lead Halide Perovskites with Improved Stability for Tandem Solar Cells. *J. Phys. Chem. Lett.* **2016**, *7*, 746−751.

(30) Braunger, S.; Mundt, L. E.; Wolff, C. M.; Mews, M.; Rehermann, C.; Jost, M.; Tejada, A.; Eisenhauer, D.; Becker, C.; Guerra, J. A.; et al. $Cs_xFA_{1−x}Pb(I_{1−y}Br_y)_3$ Perovskite Compositions: the Appearance of Wrinkled Morphology and its Impact on Solar Cell Performance. *J. Phys. Chem. C* **2018**, *122*, 17123−17135.

(31) Blöchl, P. E. Projector Augmented-Wave Method. *Phys. Rev. B: Condens. Matter Mater. Phys.* **1994**, *50*, 17953−17979.

(32) Kresse, G.; Joubert, D. From Ultrasoft Pseudopotentials to the Projector Augmented-Wave Method. *Phys. Rev. B: Condens. Matter Mater. Phys.* **1999**, *59*, 1758−1775.

(33) Perdew, J. P.; Ruzsinszky, A.; Csonka, G. I.; Vydrov, O. A.; Scuseria, G. E.; Constantin, L. A.; Zhou, X.; Burke, K. Restoring the Density-Gradient Expansion for Exchange in Solids and Surfaces. *Phys. Rev. Lett.* **2008**, *100*, 136406.

(34) Eperon, G. E.; Stranks, S. D.; Menelaou, C.; Johnston, M. B.; Herz, L. M.; Snaith, H. J. Formamidinium Lead Trihalide: A Broadly Tunable Perovskite for Efficient Planar Heterojunction Solar Cells. *Energy Environ. Sci.* **2014**, *7*, 982−988.

(35) Grimme, S.; Antony, J.; Ehrlich, S.; Krieg, H. A Consistent and Accurate Ab Initio Parametrization of Density Dunctional Dispersion Dorrection (DFT-D) for the 94 elements H-Pu. *J. Chem. Phys.* **2010**, *132*, 154104.

(36) Asenov, A.; Cathignol, A.; Cheng, B.; McKenna, K. P.; Brown, A. R.; Shluger, A. L.; Chanemougame, D.; Rochereau, K.; Ghibaudo, G. Origin of the Asymmetry in the Magnitude of the Statistical Variability of n- and p-Channel Poly-Si Gate Bulk MOSFETs. *IEEE Electron Device Lett.* **2008**, *29*, 913−915.

(37) McKenna, K. P.; Shluger, A. L. Electron-Trapping Polycrystalline Materials with Negative Electron Affinity. *Nat. Mater.* **2008**, *7*, 859−62.

(38) Bean, J. J.; Saito, M.; Fukami, S.; Sato, H.; Ikeda, S.; Ohno, H.; Ikuhara, Y.; McKenna, K. P. Atomic Structure and Electronic Properties of MgO Grain Boundaries in Tunnelling Magnetoresistive Devices. *Sci. Rep.* **2017**, *7*, 45594.

(39) von Alfthan, S.; Benedek, N. A.; Chen, L.; Chua, A.; Cockayne, D.; Dudeck, K. J.; Elsässer, C.; Finnis, M. W.; Koch, C. T.; Rahmati, B.; et al. The Structure of Grain Boundaries in Strontium Titanate: Theory, Simulation, and Electron Microscopy. *Annu. Rev. Mater. Res.* **2010**, *40*, 557−599.

(40) Imaeda, M.; Mizoguchi, T.; Sato, Y.; Lee, H. S.; Findlay, S. D.; Shibata, N.; Yamamoto, T.; Ikuhara, Y. Atomic Structure, Electronic Structure, and Defect Energetics in [001](310) Σ5 Grain Boundaries of $SrTiO_3$ and $BaTiO_3$. *Phys. Rev. B: Condens. Matter Mater. Phys.* **2008**, *78*, 1−12.